Efficient silicon solar cells with highly conductive zirconium nitride electron-selective contacts

View Online   Export Citation   CrossMark

Juan Tian,[1] Kai Xu,[2] Guangwei Wang,[1] Hongxu Jiang,[1] Yuan Liu,[3,4] Peng Zhu,[3] and Deliang Wang[1,5,a]

AFFILIATIONS

[1]Hefei National Laboratory for Physical Sciences at Microscale, University of Science and Technology of China, Hefei, Anhui 230026, People's Republic of China

[2]Nano Science and Technology Institute, University of Science and Technology of China, Suzhou, Jiangsu 215123, People's Republic of China

[3]College of Chemistry and Chemical Engineering, Nantong University, Nantong, Jiangsu 226019, People's Republic of China

[4]Jiangsu Province Cultivation base for State Key Laboratory of Photovoltaic Science and Technology, Changzhou University, Changzhou, Jiangsu 213164, China

[5] Key Laboratory of Materials for Energy Conversion, Chinese Academy of Sciences, University of Science and Technology of China, Hefei, Anhui 230026, People's Republic of China

[a]Author to whom correspondence should be addressed: eedewang@ustc.edu.cn

ABSTRACT

Efficient carrier transport and suppressed interface recombination at back contact are essential for high-efficiency solar cells. Herein, we developed a zirconium nitride (ZrN) film with a low film resistivity of 1.6×10^{-4} Ω cm as an electron-selective contact for n-type silicon solar cells. Suitable band alignment of the n-Si/ZrN hetero-contact eliminates the interface barrier between Al and n-Si. Meanwhile, electrostatic potential induced by interfacial Si–O–Zr bonds assists electron extraction. The fill factor of devices has been significantly improved by incorporating a ZrN layer. After optimizing the thickness of ZrN and contact fraction, the champion ZrN-based device exhibited an efficiency of 19.7%, yielding a 23% enhancement compared with that without a ZrN interlayer.

Excellent contact is an indispensable aspect of a high-performance solar cell. Over the past few years, advanced contact technologies for solar cells based on c-Si have been developed such as a tunnel oxide passivated contact,[1,2] which can boost solar cell efficiency remarkably and has been commercialized. Nevertheless, extra optical losses would be induced due to parasitic absorption.[3] In addition, these technologies typically involve high processing temperatures and toxic gases, leading to increased costs and even environmental concerns. In this regard, they do not meet the long-term requirements.

Dopant-free carrier-selective hetero-contacts are believed to be essential for alleviating these issues. Several groups of carrier-selective materials, including transition metal oxides,[4–7] alkali metal fluorides,[8–10] and organic films,[11,12] have been applied. However, most of them behave as insulators, so that the contact properties rely heavily on the thickness of interlayers, which narrows the process window. Recently, transition metal nitrides/oxynitrides featuring quasi-metallic characteristics are an emerging class of carrier-selective materials with significant potential for application in photovoltaic devices.[13–18]

Yang *et al.* deposited TiN films with a resistivity of 3.6×10^{-4} Ω cm. The TiN layer was employed not only as an electron-selective layer but also as an electrode material.[14] Yu *et al.* inserted a 5 nm TiN layer between Al and n-Si to lower the contact resistivity. The enhanced electron extraction was attributed to the well-matched band structure of n-Si/TiN as well as the defect states near the Fermi level of TiN.[15] Gu *et al.* reported tunable band structures in MoO_xN_y by varying the ratio of N_2:Ar during sputtering. As the N_2:Ar ratio increased, the work function of MoO_xN_y decreased, which can facilitate electron transport.[17] Although several works have demonstrated the feasibility of applying metal nitrides/oxynitrides in solar cells, research in this area is not comprehensive, and understanding of mechanisms is limited.

Being a vital member of transition metal nitrides, ZrN often serves as a diffusion barrier in the microelectronics industry because of its excellent stability. The reported values of the ZrN film resistivity range from dozens to hundreds $\mu\Omega$ cm.[19–21] The electronic band structure of ZrN is similar to that of TiN.[22] In comparison with TiN, ZrN possesses reduced dielectric losses and superior oxidation

resistance.[23–25] Furthermore, ZrN has a larger lattice constant; therefore, it is possible for the ZrN heteroepitaxy on Si substrates.[25] With these exceptional properties, the use of ZrN in optoelectronic devices has the potential to flourish. However, there have been few reports about optoelectronic devices based on ZrN. Research in relation to the carrier selectivity capability of ZrN is still scarce.

In this paper, we deposited ZrN films with a low resistivity of 1.6×10^{-4} Ω cm by sputtering from a ZrN target. The highly conductive ZrN film features high electron mobility and moderate carrier concentration. We investigated the electron selectivity and passivation property of the ZrN film on c-Si. By performing systematic micro-characterization and optoelectronic measurements, the effects of ZrN and the underlying mechanisms were studied. A series of solar cells was fabricated, and a simulation tool was utilized to provide an optimized design of the device. With a partial 5 nm ZrN/Al contact, an efficiency of 19.7% was obtained in n-type silicon cells.

ZrN films were deposited by radio frequency (RF) magnetron sputtering from a ZrN target in a pure Ar atmosphere. No substrate heating was carried out. By optimizing sputtering process parameters, a golden-yellow ZrN film deposited at 80 W and 0.3 Pa achieves a minimum film resistivity of 1.6×10^{-4} Ω cm (see the supplementary material, Fig. S1). According to Hall effect measurements, the highly conductive ZrN film possesses a high electron mobility of 3.65 cm^2/v s. We assume that the good crystallinity and the closed-packed structure are responsible for the high electron mobility of ZrN (Fig. S2). The electron concentration of 1.05×10^{22} cm^{-3} of ZrN is one order of magnitude lower than the previously used metal nitrides/oxynitrides,[14,15,17] which is beneficial for reducing parasitic absorption.[14,17]

The chemical compositions of the ZrN film were investigated using XPS measurements. Figure 1(a) demonstrates the Zr 3d

emission with and without surface etching. The mixed Lorentzian–Gaussian curves and Shirley background correction were used to fit the spectra. The Zr 3d core level consists of three doublets owing to spin-orbital splitting between Zr 3d$_{3/2}$ and Zr 3d$_{5/2}$ (a difference of 2.43 eV in the binding energy, a ratio of 3:2 in the intensity area).[26] The three Zr 3d$_{5/2}$ doublets located at 179.2, 180.4, and 181.8 eV can be assigned to Zr–N bonds, Zr–O–N bonds, and Zr–O bonds,[27] respectively. Residual oxygen during a sputtering process results in the inevitable oxidation of the ZrN film. After surface etching, only a slight change in the calculated percentages of ZrO$_x$ (from 35.9% to 29.4%) was observed, indicating the superior oxidation resistance of ZrN. It is of practical importance and shows significant potential for industrial applicability. Moreover, the non-vanishing density of states can be clearly visible within the bandgap [Fig. 1(b)]. This specific electronic structure is attributed to the weak hybridization of the nearly pure-metal Zr 4d states with N 2p states,[28] leading to quasi-metallic property of ZrN.[29] Despite having the potential to act as an efficient electron transmission channel,[15,30] the broad defect band is capable of capturing photo-generated carriers and providing plenty of recombination centers at the n-Si/ZrN interface.[31] In the meantime, plasma damage caused by sputtering would aggravate interface recombination.[17,32] A degradation in the minority carrier lifetime after ZrN is deposited on the n-Si surface [Fig. 1(c)] indicates a high recombination rate at the interface.

For investigating carrier selectivity of ZrN, structures with different contacts were fabricated. The structure diagram is illustrated in Fig. S3(a). Dark I–V characteristics, as seen in Fig. 1(d), were tested on the electrodes with the same diameter of 1.2 mm at room temperature. In the case of the n-Si substrate, the I–V curve demonstrates perfectly linear after adding ZrN, which suggests that the insertion of the ZrN
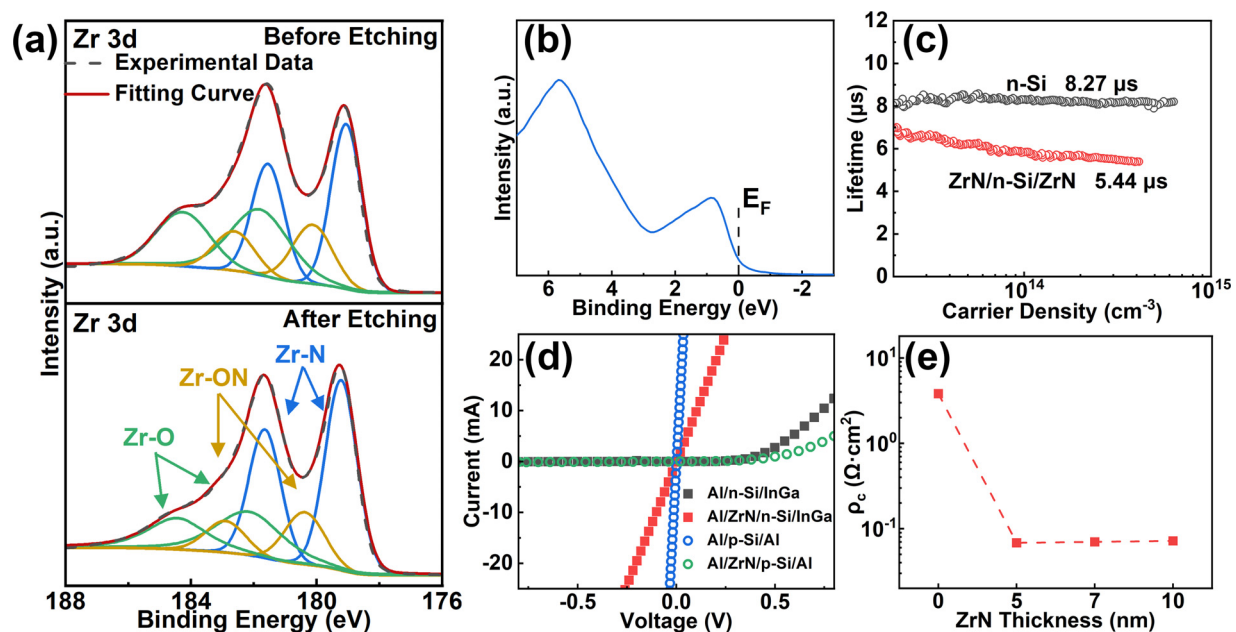

FIG. 1. (a) Zr 3d XPS spectra of the ZrN film before and after surface etching. (b) The valence band spectrum of ZrN. (c) The injection level dependent effective minority lifetime for n-Si with and without the ZrN film deposited on both sides. (d) Dark I–V curves of different structures. (e) Dependence of the contact resistivity (ρ_c) of the n-Si/ZrN/Al contact on the ZrN thickness.

film can effectively reduce the Schottky barrier height (Φ_B) of n-Si/Al and enhance electron transport. On the contrary, when the substrate is p-type silicon, I–V curves shift from Ohmic to rectifying behavior after ZrN is inserted, illustrating the hole-blocking capability of ZrN. The Cox and Strack method was adopted to acquire ρ_c of the n-Si/ZrN/Al contact, and the results are shown in Fig. 1(e).[33] By incorporating a 5 nm ZrN layer, ρ_c is significantly decreased to ~68.3 mΩ cm^2. (The detailed calculation process can be seen in Fig. S3.) We also monitored the ρ_c of samples with thicker ZrN films and found no dependence of ρ_c on the ZrN thickness. The high conductivity of ZrN reduces the ρ_c sensitivity to the interlayer thickness, providing more options for manufacturing.

To explore the underlying mechanisms of electron selectivity of ZrN, scanning Kelvin probe microscopy (SKPM), UPS, and XPS measurements have been utilized to determine the precise band alignment between n-Si and ZrN. Figure 2(a) presents the surface potential mapping, and Fig. 2(b) shows the line-scanned potential profile. After the cover of ZrN, the measured contact potential difference (CPD) increases by ~0.16 V, corresponding to a decrease in the work function. This is consistent with UPS results as shown in Fig. 2(c), as the work function is 4.26 eV for bare silicon while dropping to 4.10 eV for n-Si/ZrN. Considering the high carrier concentration of ZrN, we assume that the 0.16 eV band bending stemming from the modulation in the work function all occurs at the n-Si surface. To a hetero-structure, the valence band offset (ΔE_V) could be measured precisely with the XPS technique.[34–37] The ΔE_V of the n-Si/ZrN junction can be obtained as

$$\Delta E_V = \Delta E_{CL}(i) + \left(Si\,2p_{3/2} - VBM\right)^{bulk}_{Si} - \left(Zr\,3d_{5/2} - VBM\right)^{bulk}_{ZrN},$$
(1)

where $\left(Si\,2p_{3/2} - VBM\right)^{bulk}_{Si}$ indicates the difference between the $Si\,2p_{3/2}$ core level and the valence band maximum (VBM) obtained

from a thick n-type c-Si film and $\left(Zr\,3d_{5/2} - VBM\right)^{bulk}_{ZrN}$ indicates the difference between the $Zr\,3d_{5/2}$ core level and the VBM obtained from a thick ZrN film. $\Delta E_{CL}(i)$ is the difference between the $Zr\,3d_{5/2}$ core level and the $Si\,2p_{3/2}$ core level measured at the n-Si/ZrN interface. Detailed measurements and calculation process can be seen in Fig. S4. ΔE_V is calculated to be 2.02 eV. From the Tauc plots [Fig. S2(c)], the bandgap of the ZrN film is determined to be 3.05 eV in line with the reported values.[38] Figure 2(d) illustrates the quantitative band alignment of n-Si/ZrN based on above results. A large offset of 2.02 eV in the valence band can effectively repel holes from the back contact. Contrary to this, the downward band bending of 0.16 eV at the silicon surface and the conduction band offset of 0.09 eV enable "barrier-free" electron extraction.

The variations in surface chemical states were detected by XPS techniques. Figures 3(a) and 3(b) exhibit Si 2p and O 1s emission measured on n-Si substrates with and without ZrN coating. For the bare silicon, since the native oxide forms on the surface, the weak peak appearing at 103.00 eV is assigned to Si–O–Si bonds.[39] After the cover of 5 nm ZrN, the main Si 2p peak shifts to higher binding energies, which is associated with surface band bending of silicon as discussed above.[40] In addition, a distinct peak can be observed at 101.45 eV, suggesting the occurrence of the interfacial reaction between ZrN and Si. The O 1s peak of n-Si at 532.42 eV belongs to Si–O–Si bonds.[41] While for n-Si/ZrN, the O 1s core level exhibits a main peak at 530.17 eV accompanied by a shoulder peak at 531.75 eV. In view of the oxygen present in the ZrN film as depicted in Fig. 1(a), the peak at 530.17 eV is attributed to Zr–O bonds.[12] Noted that there is an overlap of the O 1s peaks from O–Zr–N and O–Zr–O bonds,[26] and hence, no further deconvolution is performed. By synthetically considering, we identify the signals appearing in the spectra of the n-Si/ZrN interface as Si–O–Zr bonds.[12,42] It has been proved that the charge distribution in
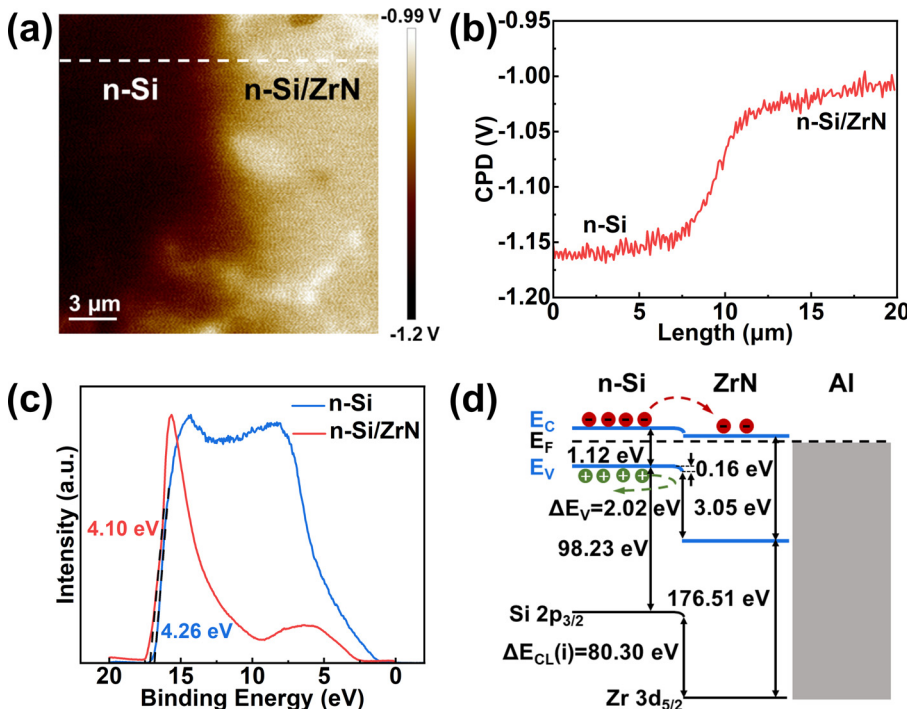

FIG. 2. (a) SKPM surface potential mapping of n-Si and 5 nm ZrN on n-Si. (b) The potential profile obtained along the line indicated in (a). (c) The UPS spectra of n-Si and n-Si/ZrN. (d) Band alignment at the n-Si/ZrN interface obtained based on the SKPM and XPS data.
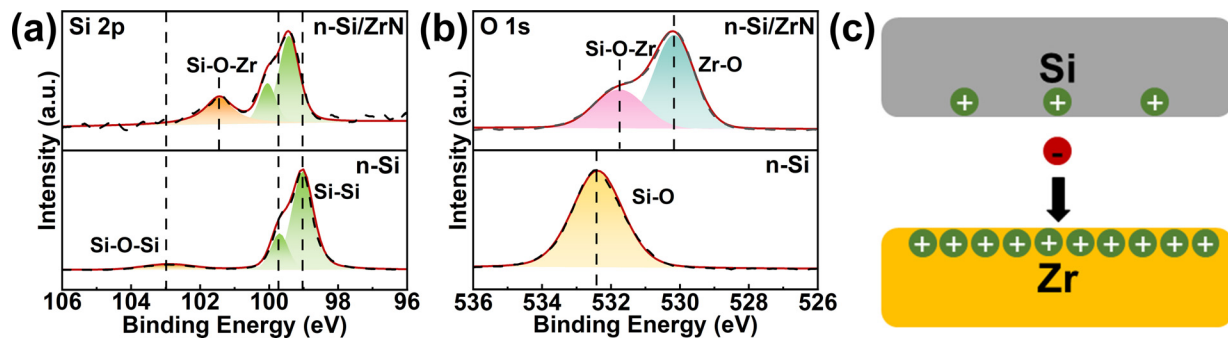
FIG. 3. (a) XPS spectra of n-Si and n-Si/ZrN: (a) Si 2p and (b) O 1s. (c) Schematic diagram of the charge distribution in Si–O–Zr.

Si and Zr is uneven when they are bonded with O.[7,43,44] Therefore, the electron transport from Si to Zr can be energetically favored by the electrostatic potential as seen in Fig. 3(c).[6,7]

N–Si-based solar cells were fabricated to examine the electron selectivity of ZrN at the device level. The detailed description of device fabrication and characterization can be seen in the supplementary material. Figure 4(a) demonstrates the light J–V characteristics and the relative parameters of devices with different back contacts. The device with a full-area 5 nm ZrN/Al electrode (labeled "5 nm ZrN/Al-100%") achieves a conversion efficiency of 17.8%, which yields an 11% enhancement compared with the device without a ZrN interlayer (labeled "Al only 100%"). This enhancement is mainly contributed by a considerable increment in the fill factor (FF) from 74.0% to 79.4%. Nevertheless, the value of V_{OC} has failed to meet expectations. As we can see, only about a 7 mV increment in V_{OC} is achieved with 5 nm

ZrN inserted. We reason that the non-ideal outcome could arise from the broad sub-bandgap defect band observed in Fig. 1(b), as well as incidental plasma damage during the sputtering process.[17,32,45] To some extent, the well-aligned band structure and the Si–O–Zr bonds, which can help separate photo-generated electron–hole pairs and passivate silicon dangling bonds, would dramatically reduce the undesirable carrier recombination. However, the high-density defects existing at the n-Si/ZrN interface make the promised gain in the passivation effect not fully realized. Figure S5 shows statistical photovoltaic parameters' evaluations on five devices fabricated with ZrN layers of varying thickness. The average values of FF exhibit no significant variation concerning the ZrN thickness, indicating that the bulk resistance of the highly conductive ZrN films has no effect on the device series resistance (R_S). This trend is well consistent with the contact resistivity results as demonstrated in Fig. 1(e). When the thickness of
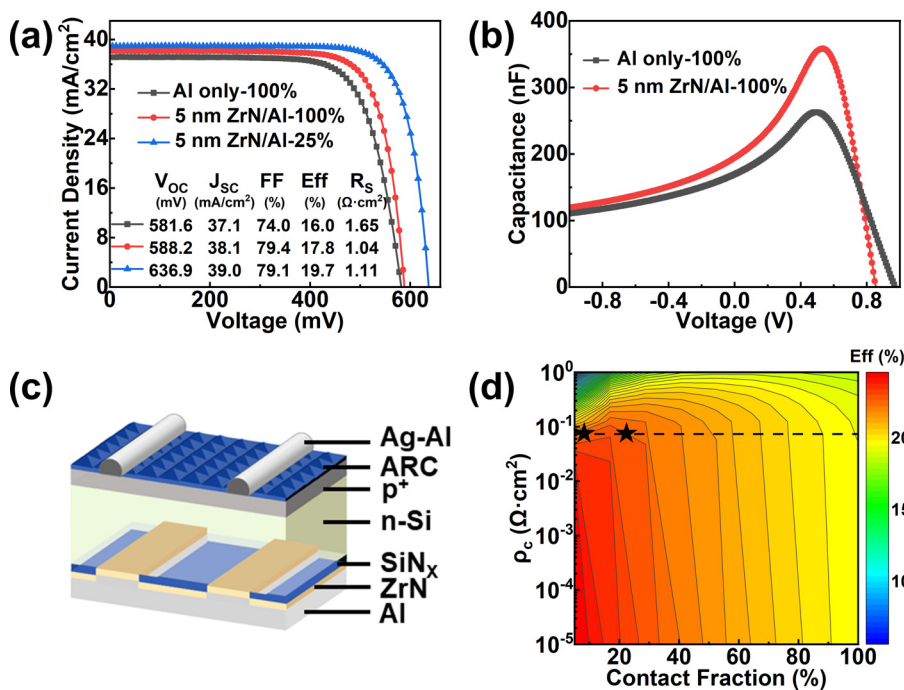

FIG. 4. (a) Light J–V curves and (b) C–V curves of solar cells with different back contacts. (c) A schematic illustration of solar cells with PRC. (d) Dependence of device efficiency on the contact resistivity and contact fraction by Quokka simulations.

ZrN exceeds 5 nm, there are small declines in the mean values of V_{OC} due to more severe plasma damage.[32,45] Noted that the average efficiencies for the solar cells with ZrN layers, no matter what ZrN thickness, are all improved in comparison with the solar cells without ZrN.

Figure 4(b) demonstrates the C–V measurements of devices with and without ZrN. A frequency of 400 kHz was used to perform C–V measurements. For the cell without ZrN, the measured capacitance is lower, and the C–V curve exhibits a slower drop at high forward bias than that with ZrN. This can be explained by a series connection of two capacitors, the p^+-emitter/n-Si main junction and the n-Si/Al Schottky diode. The applied voltage dropped both on the main junction as well as the Schottky diode.[46] The C–V characteristics disclose that the application of ZrN has resulted in a significant reduction in the back contact barrier height.

With the purpose of enhancing V_{OC}, we employed the partial rear contact (PRC) architecture. Figure 4(c) illustrates the schematic diagram of solar cells with PRC. An appropriate contact fraction is needed to enable a trade-off between excellent passivation and efficient electron transport. Simulations were run using the Quokka program to identify an optimal range of the back contact fraction.[47] Table S1 presents a summary of main input parameters. Dependence of the simulated efficiency on the back contact fraction and contact resistivity is demonstrated in Fig. 4(d). With a ρ_c of 68.3 mΩ cm^2, the optimal fraction of the 5 nm ZrN/Al contact ranges from 8% to 25% for best performance. In practice, the device hits the highest efficiency of 19.7% with the ZrN/Al contact comprising ∼25% of the back surface. The corresponding light J–V characteristic labeled "5 nm ZrN/Al-25%" is displayed in Fig. 4(a). A substantially enhanced V_{OC} of 636.9 mV confirms that a certain degree of interface passivation has been reached. Meanwhile, due to the appropriate contact fraction, the PRC design exhibits a negligible effect on electron transport.

For solar cells with a 170-μm-thick silicon absorber layer, photons whose wavelength are over 1000 nm can penetrate close to the back contact.[48] A long-pass edge filter was used to filter the AM 1.5G light source (marked as "infrared illumination" hereafter), and the light spectrum of the filter is shown in the inset of Fig. 5(a). The carrier collection at the rear contact could be reflected through the variation in FF under different illuminations.[46] The J–V characteristics obtained in the condition of infrared illumination are exhibited in Fig. 5(a). Compared to that under AM 1.5G illumination, the FFs of devices all exhibit a decrease, albeit to varying degrees. This is because a large portion of electron–hole pairs is generated near the back contact.

Carriers would like to perform a higher recombination probability than those generated near the p^+-Si/n-Si junction region. The FF of the device without a ZrN film shows the greatest decrease from 74.0% to 66.2%, whereas the FF of the device with a full-area ZrN/Al contact decreases from 79.4% to 73.6%. When the contact fraction of ZrN/Al is 25%, the FF exhibits a minimum reduction from 79.1% to 76.2%. Under infrared illumination, the FF of 5 nm ZrN/Al-25% is higher than that of 5 nm ZrN/Al-100%. Owing to the high barrier at the interface of n-Si/Al, electron–hole pairs generated near the rear surface cannot be separated immediately and are more likely to recombine. The partial ZrN/Al contact cannot only reduce the electron barrier height between n-Si and Al but also works well in decreasing the recombination losses caused by the interface defects between n-Si and ZrN. This is verified by the high V_{OC} of 565.5 mV. The dark J–V characteristics as demonstrated in Fig. 5(b) provide further evidence of the improved passivation, as the reverse saturation current density reduces by an order of magnitude after employing the PRC structure. It is proposed that the differences in J_{SC} between three devices under AM 1.5G illumination are primarily due to their diverse efficiency in collecting photons with long wavelengths. This conclusion is further substantiated by external quantum efficiency (EQE) spectra as depicted in Fig. 5(c). In future works, the optimization of the n-Si/ZrN interface is required for further enhancement in the device performance. The contact resistivity is expected to be reduced so that the contact fraction could be further confined. Strategies such as inserting a passivation layer could be developed to reduce the carrier recombination between n-Si and ZrN.

In summary, highly conductive ZrN films were integrated into silicon cells in this work. Owing to the low resistivity of the ZrN film, the values of contact resistivity are independent of the ZrN thickness. The well-matched energy alignment and the formation of Si–O–Zr bonds contribute to the electron selectivity of ZrN. At the same time, the passivation effects are hindered by the high-density interface defects. Compared with the devices without ZrN, solar cells featuring full-area 5 nm ZrN/Al contacts achieved a considerable enhancement in FF, but only a small improvement in V_{OC}. The PRC design was employed to suppress the interface recombination. To further enhance efficiency, strategies such as adding a passivation layer could be developed. This study broadens the application of metal nitrides/oxynitrides in silicon solar cells, provides further insight into the mechanisms, and offers guidance on the use of metal nitrides/oxynitrides in optoelectronic devices.
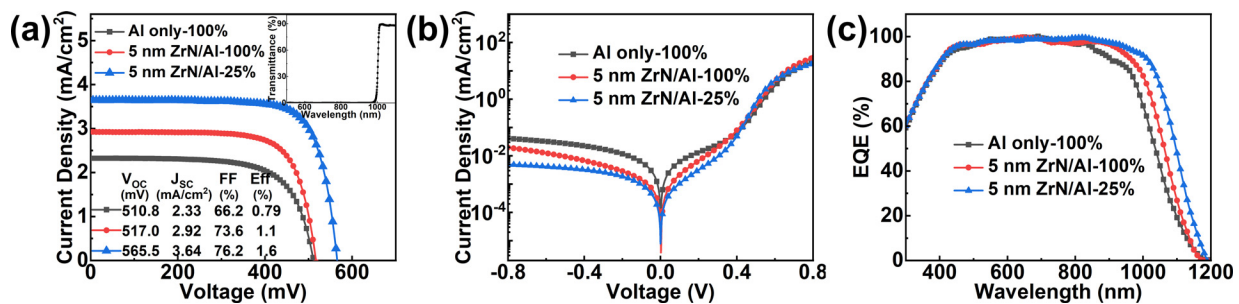

FIG. 5. (a) J–V curves of solar cells under infrared illumination. The inset shows the transmission spectrum of the long-pass edge filter. (b) Dark J–V curves and (c) external quantum efficiency (EQE) spectra of solar cells with different back contacts.

See the supplementary material for experimental details, XRD, SEM, UV-vis, XPS, film resistivity, contact resistivity, statistical photovoltaic parameters' results, and the parameters for simulation.

AUTHOR DECLARATIONS

Conflict of Interest

The authors have no conflicts to disclose.

Author Contributions

Juan Tian: Data curation (lead); Formal analysis (lead); Investigation (lead); Methodology (lead); Writing – original draft (lead). **Kai Xu:** Methodology (equal). **Guangwei Wang:** Writing – review & editing (equal). **Hongxu Jiang:** Writing – review & editing (equal). **Yuan Liu:** Conceptualization (equal); Project administration (equal). **Peng Zhu:** Conceptualization (equal); Funding acquisition (equal). **Deliang Wang:** Funding acquisition (lead); Project administration (lead).

DATA AVAILABILITY

The data that support the findings of this study are available from the corresponding author upon reasonable request.

REFERENCES

[1]F. Feldmann, M. Bivour, C. Reichel, M. Hermle, and S. W. Glunz, Sol. Energy Mater. Sol. Cells **120**, 270 (2014).
[2]F. Feldmann, M. Bivour, C. Reichel, H. Steinkemper, M. Hermle, and S. W. Glunz, Sol. Energy Mater. Sol. Cells **131**, 46 (2014).
[3]C. Messmer, A. Fell, F. Feldmann, N. Wohrle, J. Schon, and M. Hermle, IEEE J. Photovoltaics **10**, 335 (2020).
[4]Y. Wan, C. Samundsett, J. Bullock, M. Hettick, T. Allen, D. Yan, J. Peng, Y. Wu, J. Cui, A. Javey, and A. Cuevas, Adv. Energy Mater. **7**, 1601863 (2016).
[5]J. Geissbühler, J. Werner, S. M. de Nicolas, L. Barraud, A. Hessler-Wyser, M. Despeisse, S. Nicolay, A. Tomasi, B. Niesen, S. De Wolf, and C. Ballif, Appl. Phys. Lett. **107**, 081601 (2015).
[6]J. Yu, M. Liao, D. Yan, Y. Wan, H. Lin, Z. Wang, P. Gao, Y. Zeng, B. Yan, and J. Ye, Nano Energy **62**, 181 (2019).
[7]L. Chen, Z. Gao, Y. Zheng, M. Cui, H. Yan, D. Wei, S. Dou, J. Ji, E. Jia, N. Sang, K. Liu, X. Ding, Y. Li, and M. Li, Sol. Energy **174**, 549 (2018).
[8]J. Bullock, P. Zheng, Q. Jeangros, M. Tosun, M. Hettick, C. M. Sutter-Fella, Y. Wan, T. Allen, D. Yan, D. Macdonald, S. De Wolf, A. Hessler-Wyser, A. Cuevas, and A. Javey, Adv. Energy Mater. **6**, 1600241 (2016).
[9]J. Bullock, M. Hettick, J. Geissbühler, A. J. Ong, T. Allen, C. M. Sutter-Fella, T. Chen, H. Ota, E. W. Schaler, S. De Wolf, C. Ballif, A. Cuevas, and A. Javey, Nat. Energy **1**, 15031 (2016).
[10]Y. Wan, C. Samundsett, J. Bullock, T. Allen, M. Hettick, D. Yan, P. Zheng, X. Zhang, J. Cui, J. McKeon, A. Javey, and A. Cuevas, ACS Appl. Mater. Interfaces **8**, 14671 (2016).
[11]X. Shen, B. Sun, D. Liu, and S. T. Lee, J. Am. Chem. Soc. **133**, 19408 (2011).
[12]L. Yao, Z. Ying, W. Wang, Z. Yang, J. Sun, X. Wang, X. Yang, Y. Zeng, B. Yan, X. Xu, and J. Ye, Sol. Energy **215**, 410 (2021).
[13]X. Yang, E. Aydin, H. Xu, J. Kang, M. Hedhili, W. Liu, Y. Wan, J. Peng, C. Samundsett, A. Cuevas, and S. Wolf, Adv. Energy Mater. **8**, 1800608 (2018).
[14]X. Yang, W. Liu, M. De Bastiani, T. Allen, J. Kang, H. Xu, E. Aydin, L. Xu, Q. Bi, H. Dang, E. AlHabshi, K. Kotsovos, A. AlSaggaf, I. Gereige, Y. Wan, J. Peng, C. Samundsett, A. Cuevas, and S. D. Wolf, Joule **3**, 1314 (2019).
[15]J. Yu, P. Phang, C. Samundsett, R. Basnet, G. P. Neupan, X. Yang, D. H. Macdonald, Y. Wan, D. Yan, and J. Ye, ACS Appl. Mater. Interfaces **12**, 26177 (2020).
[16]X. Yang, Y. Lin, J. Liu, W. Liu, Q. Bi, X. Song, J. Kang, F. Xu, L. Xu, M. N. Hedhili, D. Baran, X. Zhang, T. D. Anthopoulos, and S. D. Wolf, Adv. Mater. **32**, e2002608 (2020).
[17]Z. Gu, L. Li, G. Du, Y. Lin, L. Lu, J. Chen, Z. Du, R. Liu, Q. Cheng, K. Gao, X. Yang, and D. Li, Appl. Phys. Lett. **120**, 123902 (2022).
[18]Y. Li, Y. Li, G. Zhang, J. Li, D. Liang, Y. Wu, T. Song, X. Yang, D. Li, C. Jiang, and B. Sun, Phys. Status Solidi (RRL) **15**, 2100159 (2021).
[19]H. M. Benia, M. Guemmaz, G. Schmerber, A. Mosser, and J.-C. Parlebas, Appl. Surf. Sci. **200**, 231 (2002).
[20]S. Inoue, K. Tominaga, R. P. Howson, and K. Kusaka, J. Vacuum Sci. Technol. A: Vacuum, Surf., Films **13**, 2808 (1995).
[21]L. Hu, D. Li, and G. Fang, Appl. Surf. Sci. **220**, 367 (2003).
[22]H. Höchst, R. D. Bringans, P. Steiner, and T. Wolf, Phys. Rev. B **25**, 7183 (1982).
[23]P. Patsalas, N. Kalfagiannis, S. Kassavetis, G. Abadias, D. V. Bellas, C. Lekka, and E. Lidorikis, Mater. Sci. Eng.: R: Rep. **123**, 1 (2018).
[24]G. Abadias, L. E. Koutsokeras, A. Siozios, and P. Patsalas, Thin Solid Films **538**, 56 (2013).
[25]P. Patsalas, Thin Solid Films **688**, 137438 (2019).
[26]T. Muneshwar and K. Cadien, Appl. Surf. Sci. **435**, 367 (2018).
[27]H. Iwata, H. Ishii, D. Kato, S. Kawashima, K. Kodama, M. Furusawa, M. Tanaka, and T. Sekiya, J. Vacuum Sci. Technol. A **36**, 061509 (2018).
[28]P. Prieto, L. Galan, and J. M. Sanz, Phys. Rev. B **47**, 1613 (1993).
[29]I. Milošev, H.-H. Strehblow, and B. Navinšek, Thin Solid Films **303**, 246 (1997).
[30]K. Shen, R. Yang, D. Wang, M. Jeng, S. Chaudhary, K. Ho, and D. Wang, Sol. Energy Mater. Sol. Cells **144**, 500 (2016).
[31]S. Lee, M. Gunes, C. R. Wronski, N. Maley, and M. Bennett, Appl. Phys. Lett. **59**, 1578 (1991).
[32]B. Demaurex, S. D. Wolf, A. Descoeudres, Z. C. Holman, and C. Ballif, Appl. Phys. Lett. **101**, 171604 (2012).
[33]R. H. Cox and H. Strack, Solid-State Electron. **10**, 1213 (1967).
[34]L. Kranz, C. Gretener, J. Perrenoud, R. Schmitt, F. Pianezzi, F. L. Mattina, P. Blosch, E. Cheah, A. Chirila, C. M. Fella, H. Hagendorfer, T. Jager, S. Nishiwaki, A. R. Uhl, S. Buecheler, and A. N. Tiwari, Nat. Commun. **4**, 2306 (2013).
[35]P. D. C. King, T. D. Veal, P. H. Jefferson, and C. F. McConville, Appl. Phys. Lett. **90**, 132105 (2007).
[36]R. Puthenkovilakam and J. P. Chang, Appl. Phys. Lett. **84**, 1353 (2004).
[37]T. P. Dhakal, S. Harvey, M. V. Hest, and G. Teeter, in *2015 IEEE 42nd Photovoltaic Specialist Conference (PVSC)* (IEEE, New Orleans, LA, 2015).
[38]Y. M. Chen, H. Q. Zhang, Z. W. Li, W. Cao, B. Liao, and X. Zhang, Surf. Eng. **29**, 567 (2013).
[39]W. M. Lau and X. W. Wu, Surf. Sci. **245**(3), 345 (1991).
[40]E. A. Kraut, R. W. Grant, J. R. Waldrop, and S. P. Kowalczyk, Phys. Rev. Lett. **44**, 1620 (1980).
[41]R. B. Shalvoy, P. J. Reucroft, and B. H. Davis, J. Catal. **56**, 336 (1979).
[42]H. Song, S. Zhao, J. Chen, and H. Qi, Microporous Mesoporous Mater. **224**, 277 (2016).
[43]J. Anderson, C. Fergusson, I. Rodriguezramos, and A. Guerreroruiz, J. Catal. **192**, 344 (2000).
[44]S.-G. Chen, Y.-S. Yin, and D.-P. Wang, J. Am. Ceram. Soc. **88**, 1041 (2005).
[45]A. H. T. Le, V. A. Dao, D. P. Pham, S. Kim, S. Dutta, C. P. T. Nguyen, Y. Lee, Y. Kim, and J. Yi, Sol. Energy Mater. Sol. Cells **192**, 36 (2019).
[46]X. Li, D. Xiao, L. Wu, D. Wang, G. Wang, and D. Wang, Sol. Energy **185**, 324 (2019).
[47]A. Fell, IEEE Trans. Electron Devices **60**, 733 (2013).
[48]M. A. Green and M. J. Keevers, Prog. Photovolt.: Res. Appl. **3**, 189 (1995).